

Lyman-tomography of cosmic infrared background fluctuations with *Euclid*: probing emissions and baryonic acoustic oscillations at $z \gtrsim 10$.

A. Kashlinsky¹, R.G. Arendt², F. Atrio-Barandela³, and K. Helgason⁴

ABSTRACT

The *Euclid* space mission, designed to probe evolution of the Dark Energy, will map a large area of the sky at three adjacent near-IR filters, Y, J and H. This coverage will also enable mapping source-subtracted cosmic infrared background (CIB) fluctuations with unprecedented accuracy on sub-degree angular scales. Here we propose methodology, using the Lyman-break tomography applied to the *Euclid*-based CIB maps, to accurately isolate the history of CIB emissions as a function of redshift from $10 \lesssim z \lesssim 20$, and to identify the baryonic acoustic oscillations (BAOs) at those epochs. To identify the BAO signature, we would assemble individual CIB maps over conservatively large contiguous areas of $\gtrsim 400 \text{deg}^2$. The method can isolate the CIB spatial spectrum by z to sub-percent statistical accuracy. We illustrate this with a specific model of CIB production at high z normalized to reproduce the measured *Spitzer*-based CIB fluctuation. We show that even if the latter contain only a small component from high- z sources, the amplitude of that component can be accurately isolated with the methodology proposed here and the BAO signatures at $z \gtrsim 10$ are recovered well from the CIB fluctuation spatial spectrum. Probing the BAO at those redshifts will be an important test of the underlying cosmological paradigm, and would narrow the overall uncertainties on the evolution of cosmological parameters, including the Dark Energy. Similar methodology is applicable to the planned *WFIRST* mission, where we show that a possible fourth near-IR channel at $\geq 2 \mu\text{m}$ would be beneficial.

Subject headings: Cosmology: miscellaneous — cosmic background radiation — cosmological parameters — dark ages, reionization, first stars — early universe — large-scale structure of universe

¹ Code 665, Observational Cosmology Lab, NASA Goddard Space Flight Center, Greenbelt, MD 20771 and SSAI, Lanham, MD 20770; email: Alexander.Kashlinsky@nasa.gov

² Code 665, Observational Cosmology Lab, NASA Goddard Space Flight Center, Greenbelt, MD 20771 and UMBC, Baltimore, MD 21250

³Dept of Theoretical Physics, University of Salamanca, Spain.

⁴MPA, Karl-Schwarzschild-Str. 1, 85748 Garching, Germany

1. Introduction

Cosmic Infrared Background (CIB) contains emissions from first sources at the end of the “Dark Ages”, individually inaccessible to telescopic studies (see review by Kashlinsky 2005). Significant development in identifying CIB fluctuations from early times came with the discovery of source-subtracted CIB fluctuations in deep *Spitzer* data (Kashlinsky et al. 2005, 2007a, 2012 - KAMM1, KAMM2, K12) which strongly exceed fluctuations from remaining known galaxies (KAMM1, Helgason et al. 2012 - HRK12). It was suggested that these fluctuations arise at epochs associated with the first-stars era (KAMM1, Kashlinsky et al. 2007b - KAMM3) or in yet undiscovered populations at low z , ripped off from their galaxies and contributing the intrahalo light (Cooray et al. 2012).

Euclid (Laureijs et al. 2011) is designed to probe evolution of the “dark energy” (DE) and provide a near-IR coverage over a substantial part of the sky. The instrumental and observational characteristics of the mission make it uniquely suitable for the near-IR CIB measurements, which this team will perform via a NASA-funded project LIBRAE (Looking at Infrared Background Radiation Anisotropies with Euclid). This *Letter* shows how tomographic analysis of the *Euclid* data, using the Lyman-break feature in the portion of the CIB from pre-reionization epochs, can 1) isolate CIB contributions as a function of z at $10 \lesssim z \lesssim 20$, and 2) probe the BAOs at those epochs.

2. Methodology and application to *Euclid* parameters

The spectral energy distribution (SED) of sources at high z exhibits a cutoff at energies above the Lyman limit (e.g. Haardt & Madau 2012). In the presence of significant amounts of neutral hydrogen (H I) such cutoff would lie at the Ly α transition of 10.2 eV (0.122 μm), while if the surrounding hydrogen were ionized (H II) the cutoff would be likely at the Ly-continuum of 13.6 eV (0.0912 μm). Because of the cutoff in the SED of populations, a filter at λ sees only sources at $z \leq z_{\text{Ly}}(\lambda) \equiv \frac{\lambda}{\lambda_{\text{Ly-break}}} - 1$ with λ always corresponding to the *longest* wavelength of the filter. z_{Ly} may vary by $\sim 20\%$ due to the Lyman-continuum vs Ly α cutoffs. Observations of the Gunn-Peterson absorption suggest presence of H I at $z \gtrsim 6 - 7$, making it likely that at $z \gtrsim 10$ the cutoff in the SED of the objects lies at Ly α (Djorgovski et al. 2003, and references therein).

After Fourier transforming CIB fluctuations, $f(\mathbf{q}) = \int \delta F(\mathbf{x}) \exp(-i\mathbf{x} \cdot \mathbf{q}) d^2x$, the (auto-)power spectrum at λ_1 is $P_1(q) = \langle |f(\mathbf{q})|^2 \rangle$, with the average taken over the independent Fourier elements corresponding to the given q . The cross-power between fluctuations at λ_1, λ_2 is $P_{12}(q) = \langle f_1(q) f_2^*(q) \rangle$. The coherence between the two bands is $\mathcal{C}_{12} \equiv \frac{P_{12}^2}{P_1 P_2} \leq 1$. The mean square fluctuation on angular scale $2\pi/q$ is $\frac{q^2 P}{2\pi}$ and the cyclical wavenumber q is related to multipole $\ell \simeq q$ (in radian $^{-1}$).

The projected CIB auto-power is related to the underlying 3-D power, P_{3D} , of the sources by the relativistic Limber equation: $P_\lambda(q) = \int \left(\frac{dF_{\lambda'}}{dz}\right)^2 Q(qd_A^{-1}; z) dz$, where d_A is the comoving angular distance to z , $Q(k, z) \equiv \frac{P_{3D}(k, z)}{c(1+z)dt/dzd_A^2(z)}$ and $\frac{dF_{\lambda'}}{dz}$ is the CIB flux production at rest $\lambda' \equiv \lambda/(1+z)$ over the epochs spanned by the integration. Assuming a flat Universe with matter,

DE, radiation/relativistic component and curvature density parameters: $\Omega_m, \Omega_{\text{DE}}, \Omega_\gamma, \Omega_k$, leads to $c(1+z)dt/dz = cH_0^{-1}/[E(z)]^{\frac{1}{2}}$ and $d_A(z) = \int_0^z dz'/E(z')$, where $E(z) \equiv \Omega_\gamma(1+z)^4 + \Omega_m(1+z)^3 + \Omega_k(1+z)^2 + \Omega_{\text{DE}}f(z)$, with $f(z)$ describing the z -evolution of DE. Then the mean squared flux fluctuation at λ can be rewritten as:

$$\frac{q^2 P_\lambda(q, < z_{\text{Ly}}(\lambda))}{2\pi} = \int_0^{z_{\text{Ly}}(\lambda)} \left(\frac{dF_{\lambda'}}{dz} \right)^2 \Delta^2(qd_A^{-1}; z) E(z) dz \quad (1)$$

where $\Delta^2(k, z) \equiv \frac{k^2 P_{3D}(k, z)}{2\pi c H_0^{-1}}$ is the mean squared fluctuation in the source counts over a cylinder of diameter k^{-1} and length $R_H \equiv cH_0^{-1}$ (Kashlinsky 2005). *The integration range stops at $z_{\text{Ly}}(\lambda)$ because sources at larger redshifts emit only longward of $\lambda_{\text{Ly-break}}$, corresponding to the far edge of the filter of band λ . The cross-power between two bands, $\lambda_2 > \lambda_1$, extends only to $z_{\text{Ly}}(\lambda_1)$:*

$$P_{12} = \int_0^{z_{\text{Ly}}(\lambda_1)} \frac{dF_{\lambda_1}}{dz} \frac{dF_{\lambda_2}}{dz} Q(qd_A^{-1}; z) dz. \quad (2)$$

For $\lambda_2 > \lambda_1$, we write:

$$P_2(q, < z_{\text{Ly}}(\lambda_2)) = \int_{z_{\text{Ly}}(\lambda_1)}^{z_{\text{Ly}}(\lambda_2)} \left(\frac{dF_{\lambda_2}}{dz} \right)^2 Q(qd_A^{-1}; z) dz + P_2(q, < z_{\text{Ly}}(\lambda_1)) = P_{\Delta z} + \frac{1}{\mathcal{C}_{12}(z < z_{\text{Ly}}(\lambda_1))} \frac{P_{12}^2}{P_1}. \quad (3)$$

$P_{\Delta z}$ above probes emissions spanning Δz at $z_{\text{Ly}}(\lambda_1) < z < z_{\text{Ly}}(\lambda_2)$ and arises from populations inaccessible to λ_1 , but present at λ_2 .

We seek to isolate the power, $P_{\Delta z}$, from luminous sources between $z_{\text{Ly}}(\lambda_1)$ and $z_{\text{Ly}}(\lambda_2)$. We rewrite (3) to isolate CIB fluctuation at $z_{\text{Ly}}(\lambda_1) < z < z_{\text{Ly}}(\lambda_2)$:

$$\frac{q^2 P_{\Delta z}(q)}{2\pi} = \left[\frac{q^2}{2\pi} \left(P_2 - \frac{P_{12}^2}{P_1} \right) \right]_{\text{data}} + \frac{q^2}{2\pi} P_{\text{sys}} \quad (4)$$

where the first rhs term is fully given by the data and the last term is driven by incoherence of the sources at the two adjacent bands which occupy the *same* span of redshifts $z < z_{\text{Ly}}(\lambda_1)$:

$$\frac{q^2}{2\pi} P_{\text{sys}} = \left[\frac{\mathcal{C}_{12}(q, z < z_{\text{Ly}}(\lambda_1)) - 1}{\mathcal{C}_{12}(q, z < z_{\text{Ly}}(\lambda_1))} \right] \times \left[\frac{q^2}{2\pi} \frac{P_{12}^2}{P_1} \right]_{\text{data}} \leq 0. \quad (5)$$

The subscript ‘‘data’’ refers to directly measurable quantities. $P_{\text{sys}} \leq 0$ because $0 \leq \mathcal{C} \leq 1$. Thus, the measurable quantity $\Delta P_{\text{obs}} \equiv (P_2 - \frac{P_{12}^2}{P_1})$ sets an *upper* limit on the CIB fluctuations arising at $z_{\text{Ly}}(\lambda_1) < z < z_{\text{Ly}}(\lambda_2)$. This methodology has already been successfully applied to deep *Spitzer* data, leading to interesting upper limits on emissions at $30 \lesssim z \lesssim 40$ (Kashlinsky et al. 2015 - K15).

Euclid’s NISP instrument will have three near-IR filters which are referred below as Y, J, H in order of increasing central wavelength: 1.056, 1.368, 1.772 μm . Each band will be available for evaluating CIB fluctuations. Figure 1a shows that the *currently* envisaged Y, J, H filters (K. Jahnke, 08/2015, private communication) isolate emissions over narrow ranges, $\sim 5-7\%$, in d_A . We

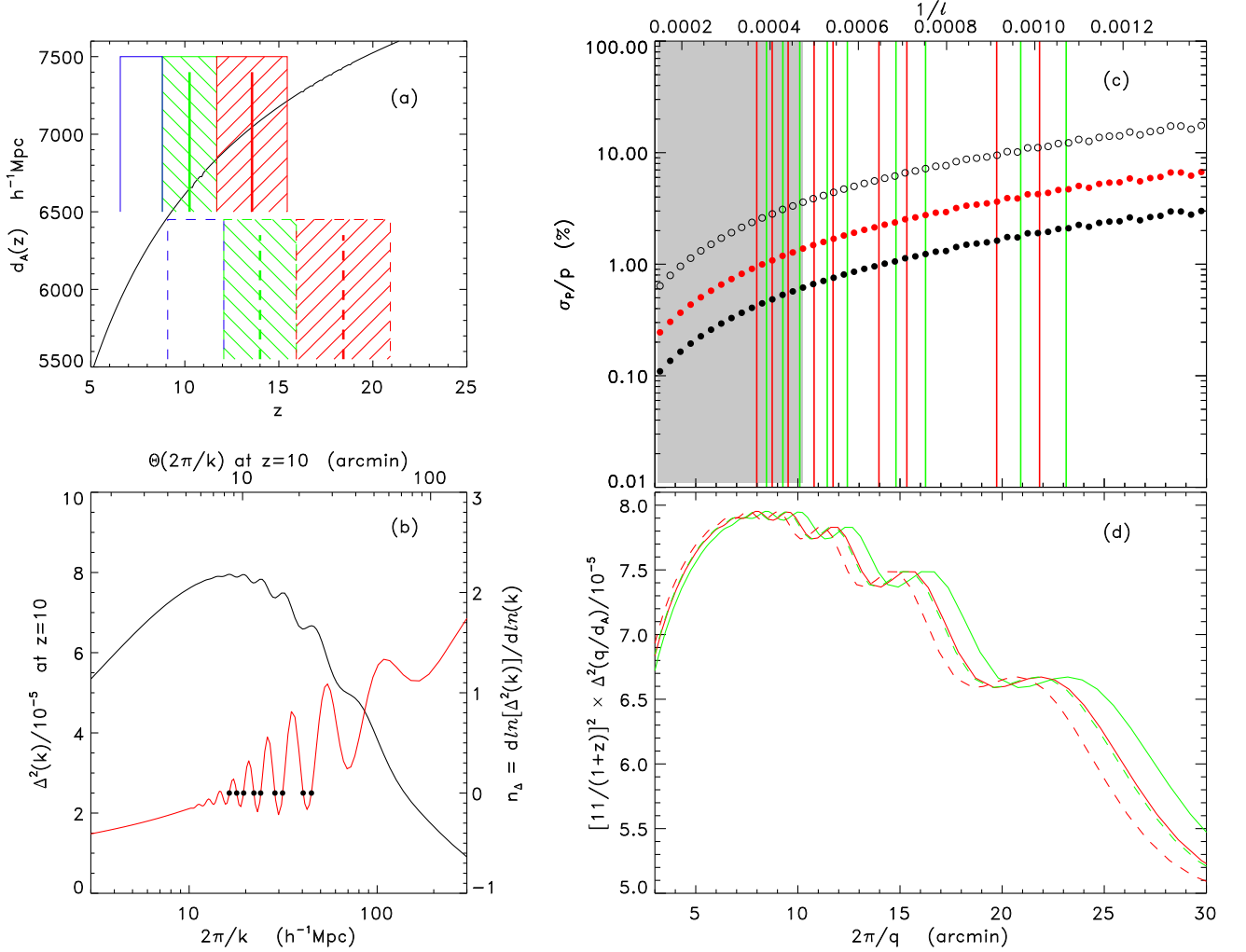


Fig. 1.— (a) Solid line shows d_A span vs z for flat Universe with $\Omega_m = 0.3, \Omega_\Lambda = 0.7$. The span of z_{Ly} over Y, J, and H *Euclid* filters is shown in blue, green, and red; vertical lines correspond to the central wavelength of each filter. Upper regions correspond to the Lyman-break at Ly- α and lower (dashed) at Ly-continuum. (b) Solid line shows $\Delta^2(k)$ evaluated with CMBFAST at $z = 10$. Red line and right axis show the spatial spectral index, n_Δ , of $\Delta^2(k)$; solid dots mark extrema of $\Delta^2(k)$. For Harrison-Zeldovich regime $n_\Delta = 3$ which is reached at larger scales. (c) Relative accuracy for probing the tomographically measured power at each angular frequency. Open, red and black filled circles correspond to selecting a $21^\circ \times 21^\circ$ deg field, 1yr and full *Euclid* Wide Survey areas. Shaded region shows the angular scales covered by one *Euclid* detector. Vertical lines mark the BAO extrema in Δ^2 for J–Y (green) and H–J tomographic maps. (d) $\Delta^2(q/d_A)$ at the redshifts marked with vertical lines in (a).

assume that at these epochs the power spectrum of the emitting sources is proportionally related to the underlying ΛCDM one: $\Delta^2(q/d_A) = b^2(z)\Delta_{\Lambda\text{CDM}}^2(q/d_A)$ with b being the bias factor, since the

relevant angular scales subtend tens of comoving Mpc where density field was highly linear. Because the procedure isolates a narrow shell in $d_A(z)$ around d_0 , the comoving angular distance to the central filter wavelength, we further expand $\Delta_{\Lambda\text{CDM}}^2(q/d_A) \simeq \Delta_{\Lambda\text{CDM}}^2(qd_0^{-1})\{1 - n_\Delta(qd_0^{-1})[\frac{d_A(z)-d_0}{d_0}]\}$, where $n_\Delta(k) \equiv d \ln \Delta_{\Lambda\text{CDM}}^2(k)/d \ln k$ is the spatial spectral index of the ΛCDM template shown in Figure 1b. Further noting that $d_A - d_0 \simeq cH_0^{-1}(z - z_0)/E(z)$ we write the power from sources over the narrow range of epochs defined in Figure 1a as:

$$\frac{q^2 P_{\Delta z}}{2\pi} \simeq \Delta_{\Lambda\text{CDM}}^2(qd_0^{-1}) \times \int_{z_{Ly}(\lambda_1)}^{z_{Ly}(\lambda_2)} \left(\frac{dF_{\lambda_2}}{dz} \right)^2 b(z)^2 \left[E(z) - n_\Delta(qd_0^{-1}) \frac{R_H}{d_0}(z - z_0) \right] dz. \quad (6)$$

This relates $P_{\Delta z}$ to the underlying parameters over the narrow range of z . Figure 1b shows the underlying shape of $\Delta^2(k)$ with the BAO oscillations being prominent at potentially measurable levels. The integration in (6) represents a convolution of the BAO spectrum over the redshift range defined by the wavelengths λ_1 and λ_2 . For λ_1 and λ_2 set by the red edges of the Y, J, and H filters, this convolution alters the amplitude of the power spectrum by $< 1\%$ if dF/dz is constant across the band.

3. Analysis configuration and uncertainties

After 6.25 years, *Euclid's* Wide Survey (EWS) will cover 15,000 deg^2 at Y, J, H to $m_{\text{AB}} \simeq 25$ (3σ); *Euclid's* Deep Survey (EDS) will cover (non-contiguously) 40 deg^2 two magnitudes deeper. The derived Y, J, and H CIB maps will be used in the tomographic reconstruction, [J–Y] and [H–J], isolating populations over $\delta d_A \ll d_A$ (Figure 1a). Equation (6) shows that scatter around the expected ΛCDM template at an effective d_A caused by the finite range in z probed in each of the tomographic constructions, will be generally small and even further reduced around the extrema of the template (Figure 1b,c). Figure 1d shows the expected angular spectra of the CIB fluctuations with BAO structures.

There are two criteria here: 1) does the measured signal fit the expected ΛCDM template?; and if it does 2) how well can the physically important parameters of that template be measured from the data?

The first criterion requires sampling the power with sufficient angular resolution, say $\Delta\theta \sim 0.5'$, at scales of $5' \leq \theta = 2\pi/q \lesssim 25'$ where the BAO structure lies. In terms of angular frequency, this means $\Delta q = 2\pi\Delta\theta/\theta^2 \approx \frac{1}{200} \text{amin}^{-1}$. The frequency resolution, Δq is set by maximum size, Θ_0 , of the region being analyzed: $\Delta q = 2\pi/\Theta_0$. Therefore, to achieve sufficient sampling to resolve the BAO structures, the analysis requires regions that are $\Theta_0 = 2\pi/(5 \times 10^{-3} \text{amin}^{-1}) \approx 21^\circ$ in size. Masking out resolved sources introduces small-scale coupling increasing Θ_0 further, although this effect would be small when probing power at $\Delta\theta \simeq 0.5'$. If so, the large value of Θ_0 requires use of EWS rather than EDS, potentially necessitating spherical harmonic analysis. However, this conservative estimate can be relaxed if the data show BAO structure dominated by emissions from one effective z . In that case, EDS' smaller fields, with lower CIB from remaining galaxies, may also

prove useful. To sample each of N_a (~ 4) acoustic peaks with $N_{\text{sampling}} > 2$ points/peak between $2\pi/25' \leq q \leq 2\pi/5'$ will lead to $\Delta q = 2\pi(\frac{1}{5'} - \frac{1}{25'}) (N_a N_{\text{sampling}})^{-1} \simeq 2\pi/250'$, or $\Theta_0 \sim 4^\circ$ for $N_a N_{\text{sampling}} = 40$.

Once the auto- and cross-power spectra are measured between channels 1 and 2 (Y and J, J and H) the quantity to be determined is ΔP_{obs} , which is to be compared to $P_{\Delta z}$. The relative accuracy on this quantity can be evaluated as sampling (cosmic) variance or $\sigma_P/P = \sqrt{6/N_q}$ with N_q being the number of independent Fourier elements that go into determining the power at each q (K15). The amplitude of the Λ CDM fit, F_0 , can be evaluated iteratively from smaller angular scales in conjunction with d_A determined from larger scales; we assume that scales $2\pi/q > 1'$ are left to evaluate the effective d_A and its uncertainty from linear least-squares regression. We model the observationally determinable $q^2 \Delta P_{\text{obs}} / (2\pi)$ as $M_i = T(q_i/d_A) + M_{\text{sys}}(q_i)$ where M_{sys} is given by Equation (5) and $T(k) = F_0^2 \Delta_{\Lambda\text{CDM}}^2(k)$. This theoretical fit model is inherently highly-nonlinear. Once data (\vec{D}) are available, Markov chain processing may be used to evaluate the range of cosmological parameters and their uncertainties. To estimate the uncertainty on d_A we 1) note the narrow width of the surface where the sources contributing to $P_{\Delta z}$ are located, 2) make an initial guess $d_A = d_0$, and 3) then linearize the model $M_i \simeq T(q_i/d_0)[1 - n_\Delta(q_i/d_0)\epsilon_d] + M_{\text{sys}}(q_i)$ with $\epsilon_d = (d - d_0)/d_0$. The result is then obtained by minimizing $\chi^2 = \langle \frac{(D_i - M_i)^2}{\sigma_i^2} \rangle$ with σ_i shown in Figure 1c. The statistical uncertainty on the distance determination from $\partial\chi^2/\partial\epsilon_d = 0$ is then:

$$\sigma_\epsilon^2 = \sum_i \left(\frac{\partial\epsilon_d}{\partial D_i} \right)^2 \sigma_i^2 = \frac{6}{\sum_i [n_\Delta(q_i/d_0)]^2 N_{q,i}} \quad (7)$$

Assuming $1' < 2\pi/q < 25'$ leads to d_A being probed with a relative accuracy of 1.25% from a single field of 400 deg^2 (as in Figure 1c). Scales $1' - 10'$, which lie entirely within one detector, account for about 90% of this. In larger EWS areas the relative uncertainty will improve $\propto 1/\sqrt{\text{area}}$. Systematic uncertainty is given by the last term in M_i ; its amplitude is illustrated in the following section.

Diffuse light fluctuations from remaining galaxies and foregrounds may contribute, although at *Spitzer* wavelengths they are much lower than the CIB fluctuation (KAMM1, HRK12, K12); additionally, they should be highly coherent. We discuss the contributions from the known remaining galaxies in the EWS in the next section. The estimated power from the zodiacal light and diffuse Galactic light (DGL) are at similar levels to that of the remaining known galaxies (KAMM1, AKMM, and K15). These foregrounds will affect the measured ΔP_{obs} at a similar level as the remaining known galaxies, provided they have comparably high coherence. The Kelsall et al. (1998) zodiacal light model suggests a color gradient of $\lesssim 0.1\%$ per degree is present between the *Euclid* bands. Measured color variations of the DGL can reach factors of 2 between different locations (Ienaka et al. 2013), indicating relatively low coherence and a stronger contribution to ΔP_{obs} on large angular scales.

4. Modelling astrophysical applications

This method applied to large contiguous areas of EWS can 1) accurately isolate the history of emissions at $10 \lesssim z \lesssim 20$ and 2) measure the BAO at those epochs. The discussion above shows that if the CIB produced by pre-reionization sources is high enough to be directly measurable with *Euclid*, both of these goals can be achieved. In this section we illustrate the feasibility of these goals with a specific model for high- z evolution in the presence of CIB from known galaxy populations that will be remaining in the *Euclid* data. The high- z modeling, while consistent with all current data, is used for illustrative, not predictive purposes.

The model adopted here for illustrative purposes is IMF500 described in detail in Helgason et al. (2015). We assume that dark matter halos collapse to form the stars with a fixed efficiency f_* until z_{end} with the rate of collapsed dark halos fixed by the power spectrum evolution in the Λ CDM model; the levels of the CIB left behind by these sources are varied via f_* . For $f_* = 0.04$ ($z_{\text{end}} = 10$) ($f_* = 0.03$ for $z_{\text{end}} = 8$) the model reproduced the source-subtracted CIB fluctuation measured in the *Spitzer* data by K12; lowering f_* would reduce the CIB fluctuation power $\propto f_*^2$. The CIB fluctuation of remaining known galaxies in EWS is calculated using the HRK12 reconstruction technique for three limits: the default reconstruction, which is supported by the later measured *Spitzer* deep counts data (Ashby et al. 2013, 2015), and two extreme limits of possible extrapolation of the observed luminosity functions, termed the high-faint-end (HFE) and low-faint-end (LFE) limits. The HRK12 empirical reconstruction employs an assembled extensive database of galaxy luminosity functions spanning a wide range of wavelengths, redshifts and luminosities; it was demonstrated to agree well with both galaxy counts from visible to near-IR and numerical modeling of galaxy evolution.

4.1. Isolating emissions at $z \gtrsim 10$

Figure 2a shows the *Spitzer*-based source-subtracted CIB fluctuations (K12) at 3.6 and 4.5 μm compared with the high- z sources in the above modeling. Presently there is no direct evidence that the measured fluctuations originate at high- z , although they appear uncorrelated at any significant level with diffuse visible-band light from sources at $m_{\text{AB}} > 28$ (Kashlinsky et al. 2007c). Providing such evidence directly from direct Lyman-break CIB measurements requires eliminating sources to much fainter limits than is possible with current experiments and will be achievable with *JWST* and *Euclid* (K15). We model the possibility of only a fractional power contributed to the measured CIB by lowering f_* ; e.g. if $f_* = 0.01$ only $\sim 6\%$ of the measured CIB power (Figure 2a) arises at high z .

To estimate how well we would recover the emissions from the z -interval defined by each adjacent filter pair, we construct each of the auto- and cross-power spectra to combine the contributions from the high- z model populations and known galaxies remaining in the EWS. The CIB fluctuation contributions from the known galaxies remaining in each *Euclid*/NISP filter for EWS are shown in

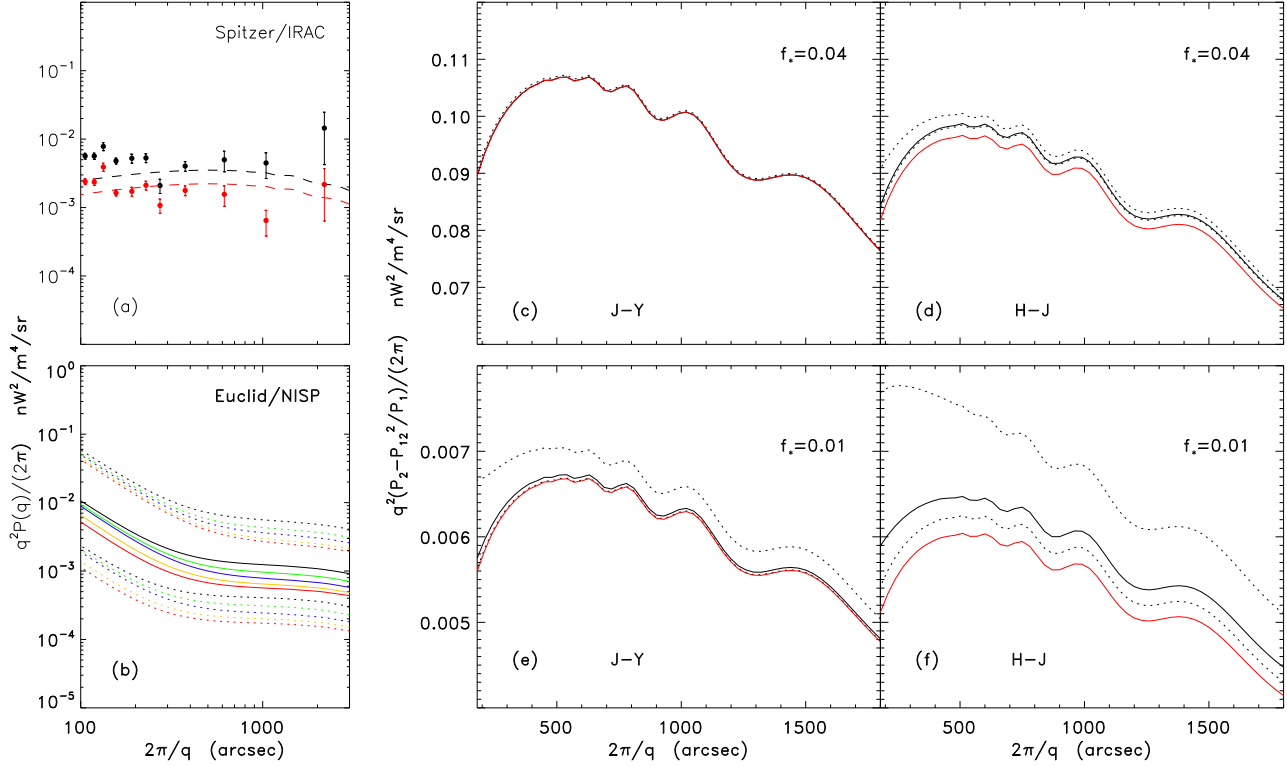


Fig. 2.— (a) *Spitzer* data at 3.6 (black) and 4.5 (red) μm (K12). IMF500 model described in the text is shown with dashed lines at $f_* = 0.04$ for $z_{\text{end}} = 10$ ($f_* = 0.03$ for $z_{\text{end}} = 8$). (b) HRK12 reconstructed CIB fluctuation from galaxies remaining unresolved in NISP data. Black, blue, red, green, yellow correspond to Y, J, H and J \times Y, H \times J configurations. Solid lines of each color correspond to the default reconstruction and dashes show the range of HFE to LFE extrapolations of the luminosity function data. (c)-(f) reconstructed $q^2 \Delta P_{\text{obs}} / (2\pi)$ from the high- z model plus the remaining galaxies at levels shown in (b): solid lines for the default reconstructions and dotted lines for the HFE (upper) and LFE limits. Red lines show the underlying CIB fluctuation produced at $z_1 < z < z_2$.

Figure 2b for the default, HFE and LFE reconstructions. For given f_* , we construct the quantity ΔP_{obs} for each of the J-Y and H-J configurations and compare it with the directly computed $P_{\Delta z}$ due to emissions over the width of the J and H filters (Figure 1a).

Figure 2c-f compares the CIB fluctuations recovered by the proposed tomography method (black lines) with the true signal produced over the given Δz (red solid). The figure illustrates that if the entire CIB signal discovered in *Spitzer*-based measurements (KAMM1, KAMM2, K12) originates at high z , this method reconstructs emission history with high accuracy (better than 6% for this illustrative model). Even if only a fraction ($\sim 6\%$ for this model) of the signal comes from high z , the accuracy remains interestingly high (better than $\sim 20\%$ for this model).

4.2. Probing BAO at $z \gtrsim 10$

While there appears a small upward bias in the emissions’ amplitude (typically $\lesssim 10\%$) estimated by this method, the recovered angular shape of the CIB fluctuations (black lines) is in very good agreement with the true angular profile (red). This is shown in Figure 3 which plots the resultant 2-D CIB power index $\tilde{n}_{\Delta z} \equiv \partial \ln[q^2 \Delta P_{\text{obs}}] / \partial \ln q$. Even for the highly pessimistic case of HFE reconstruction and $f_* = 0.01$, the ratio of the black to red lines remains constant at large scales of $\gtrsim 10'$. This argues for good prospects of BAO measurement at these epochs from the application of the Lyman tomography method to the upcoming *Euclid* CIB maps which will provide an important consistency check of the standard cosmological model.

The sound horizon at the end of the radiation drag is a (BAO) scale imprinted in P_{3D} . BAOs allow us to measure the angle subtended by the scale, which is directly related to d_A . The power spectra of Figure 2 can be used to estimate the angular size subtended by the measured sound horizon scale, $r_s = 144.81 \pm 0.24$ Mpc (Planck Collaboration 2014) as described in Percival et al. (2010). With the proposed tomography we can potentially determine $d_A(z)$ to $\lesssim 1\%$ accuracy, but with a systematic uncertainty on z due to the Lyman-break position. Eisenstein et al. (1998) proposed to constrain cosmological parameters using BAO measurements (e.g. Weinberg et al. 2013). Figure 4a plots d_A for different values of the DE equation-of-state parametrization $\omega_{\text{DE}}(z) = \omega_0 + \omega_a z / (1 + z)$ (Chevalier & Polarski 2001, Linder 2003). Triangles with red horizontal bars correspond to the proposed Lyman tomography CIB analysis of EWS. The vertical error bars (barely noticeable) correspond to 1% relative errors. Horizontal lines represent the redshift span of the CIB sources given in Figure 1a at the Ly α -break. The data will constrain cosmological parameters at $z \gtrsim 10$. *WFIRST* (Spergel et al. 2015) will carry out complementary observations to those of *Euclid*. In Figure 4a the green triangle shows the advantage of adding a *WFIRST* filter covering $2 - 2.4 \mu\text{m}$ that could provide the BAO scale at an additional z with this methodology. For comparison, we plot data from Hemantha et al. (2014) and Wang (2014) at low z . In Figure 4b we derived the confidence contours on the parameters $(\Omega_{\text{DE}}, \omega_0)$, assuming $\omega_a = 0$. The width of the contours is dominated by the finite span of z . While the method may not constrain those parameters as well as other techniques, it extends the BAO regime to hitherto unprobed z and provides an important self-consistency check. Alternatively, if the cosmological model is assumed, one can compare the measured d_A with the expected value at different z to determine the effective redshift of the sources that contribute to each of the three measurements of Figure 4a. A 0.2% (1%) relative error on the BAO angular diameter distances allows determination of d_A with an accuracy $\Delta z = 0.09, 0.15, 0.2$ (0.45, 0.75, 1), respectively. These uncertainties can be further reduced if the cross-correlation of CIB fluctuations and CMB temperature anisotropies, which are also potentially sensitive to BAOs (Atrio-Barandela & Kashlinsky 2014), is measured.

We thank Jason Rhodes for comments, Alexander Vassilkov for discussion of statistical treatment and NASA/12-EUCLID11-0003 “LIBRAE: Looking at Infrared Background Radiation Anisotropies with Euclid” for support. FAB acknowledges the Ministerio de Educacion y Ciencia project

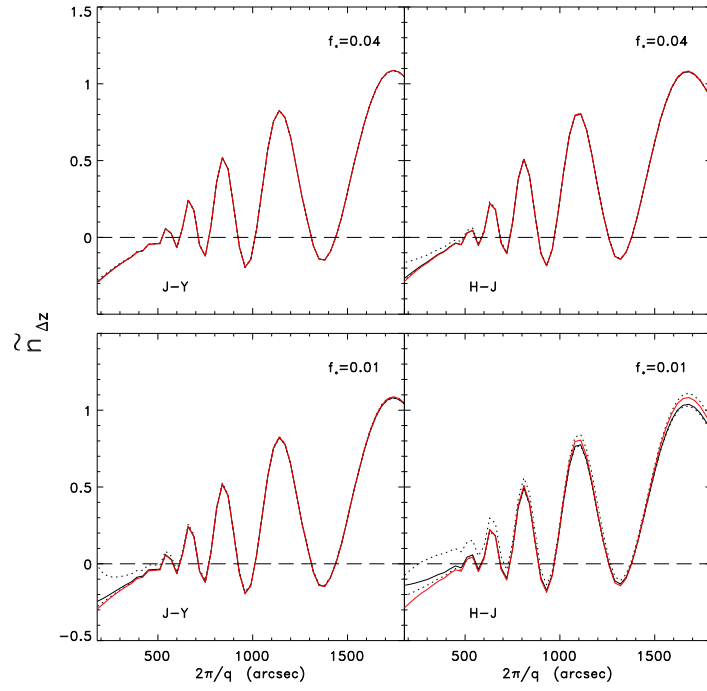


Fig. 3.— The effective CIB spatial spectral index at $[z_1, z_2]$ from ΔP_{obs} (black) vs $P_{\Delta z}$ (red). Same line notation as in Figures 2c-f.

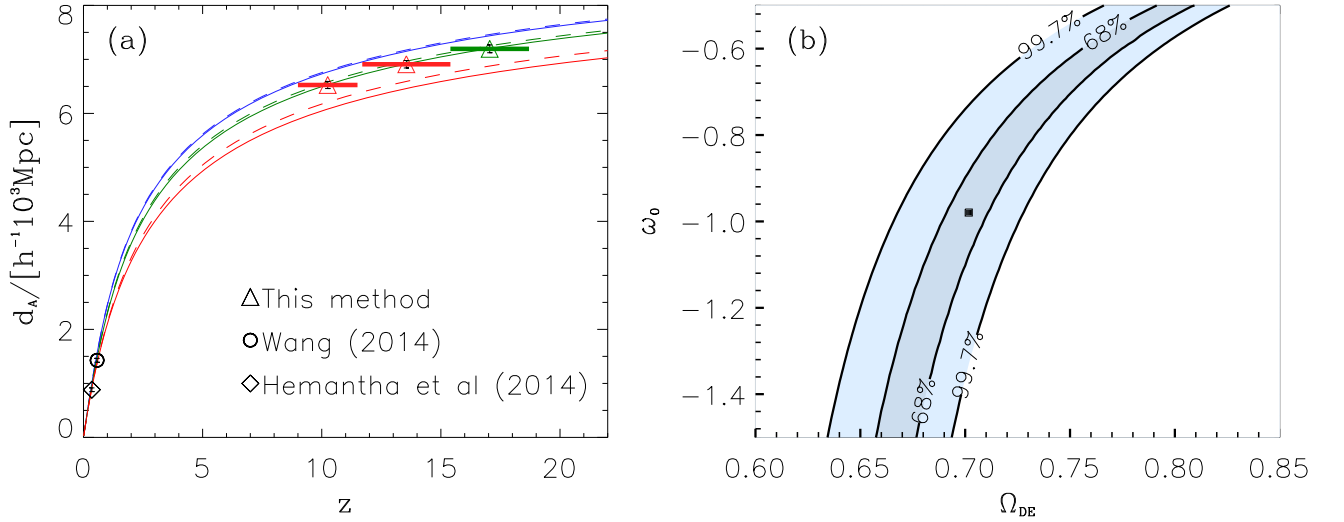


Fig. 4.— (a) d_A with DE evolving according to the CPL EoS parametrization. Blue-top, green-middle and red-bottom lines correspond to $\omega_0 = [-1.4, -1, -0.6]$. Solid/dashed lines denote $\omega_a = [-0.03, -0.3]$. Diamond and circle symbols correspond to current data and triangles to this methodology applied to *Euclid*'s (red) CIB and potentially an additional *WFIRST* (green) measurement; horizontal bars span the uncertainty in z for each *Euclid* filter configuration. (b) Confidence contours obtained from BAO measured at the three different redshifts given in (a). The black square corresponds to the best fit value; in this case the fiducial concordance model.

FIS2012-30926 and KH from EU’s 7th Framework Programme (FP7-PEOPLE-2013-IFF).

REFERENCES

- Ashby, M. L. N., Willner, S. P., Fazio, G. G., et al. 2013, *ApJ*, 769, 80
- Ashby, M. L. N., Willner, S. P., Fazio, G. G., et al. 2015, *ApJS*, 218, 33
- Atrio-Barandela, F. & Kashlinsky, A. 2014, *ApJ*, 797, L26
- Chevallier, M. & Polarski, D. 2001, *International Journal of Modern Physics D*, 10, 213
- Cooray, A., Smidt, J., de Bernardis, F., et al. 2012, *Nature*, 490, 514
- Djorgovski, G., Bogosavljevic, M. & Mahabal, A. 2003, *New Astron Reviews*, 50, 140
- Eisenstein, D. J., Hu, W. & Tegmark, M. 1998, *ApJ*, 504, L57
- Haardt, F. & Madau, P. 2012, *ApJ*, 746, 125
- Helgason, K., Ricotti, M. & Kashlinsky, A. 2012, *ApJ*, 752, 113 (HRK12)
- Helgason, K., Ricotti, M., Kashlinsky, A., & Bromm, V. 2015, *MNRAS*, in press. arXiv:1505.07226
- Hemantha, M. D. P., Wang, Y. & Chuang, C. H. 2014, *MNRAS*, 445, 3737
- Ienaka, N., Kawara, K., Matsuoka, Y., et al. 2013, *ApJ*, 767, 80
- Kashlinsky, A. 2005, *Phys. Rep.*, 409, 361
- Kashlinsky, A., Arendt, R.G., Mather, J., & Moseley, S.H. 2005, *Nature*, 438, 45 (KAMM1)
- Kashlinsky, A., Arendt, R.G., Mather, J., & Moseley, S.H. 2007a, *ApJ*, 654, L5 (KAMM2)
- Kashlinsky, A., Arendt, R.G., Mather, J., & Moseley, S.H. 2007b, *ApJ*, 654, L1 (KAMM3)
- Kashlinsky, A., Arendt, R.G., Mather, J., & Moseley, S.H. 2007c, *ApJ*, 666, L1 (KAMM4)
- Kashlinsky, A. Arendt, R., Ashby, M., Fazio, G., Mather, J. & Moseley, H. 2012, *ApJ*, 753, 63 (K12)
- Kashlinsky, A., Mather, J., Helgason, K., Arendt, R., Bromm, V. & Moseley, S.H. 2015, *ApJ*, 804, 99 (K15)
- Kelsall, T., Weiland, J. L., Franz, B. A., et al. 1998, *ApJ*, 508, 44
- Laureijs, R., Amiaux, J., Arduini, S., et al. 2011, arXiv:1110.3193
- Linder, E. V. 2003, *PRL*, 90, 091301

Planck Collaboration, Ade, P. A. R., Aghanim, N., et al. 2014, *A&A*, 571, A16

Percival, W. J., Reid, B. A., Eisenstein, D. J. et al. 2010, *MNRAS*, 401, 2148

Spergel, D., Gehrels, N., Baltay, C., et al. 2015, [arXiv:1503.03757](https://arxiv.org/abs/1503.03757)

Wang Y. 2014, *MNRAS*, 443, 2950

Weinberg, D. H., Mortonson, M. J., Eisenstein, D. J., et al. 2013, *Phys. Rep.*, 530, 87